

Multi-Scale Energy (MuSE) plug & play framework for inverse problems

Jyothi Rikhab Chand, Mathews Jacob

Abstract—We introduce a multi-scale energy formulation for plug and play (PnP) image recovery. The main highlight of the proposed framework is energy formulation, where the log prior of the distribution is learned by a convolutional neural network (CNN) module. The energy formulation enables us to introduce optimization algorithms with guaranteed convergence, even when the CNN module is not constrained as a contraction. Current PnP methods, which do not often have well-defined energy formulations, require a contraction constraint that restricts their performance in challenging applications. The energy and the corresponding score function are learned from reference data using denoising score matching, where the noise variance serves as a smoothness parameter that controls the shape of the learned energy function. We introduce a multi-scale optimization strategy, where a sequence of smooth approximations of the true prior is used in the optimization process. This approach improves the convergence of the algorithm to the global minimum, which translates to improved performance. The preliminary results in the context of MRI show that the multi-scale energy PnP framework offers comparable performance to unrolled algorithms. Unlike unrolled methods, the proposed PnP approach can work with arbitrary forward models, making it an easier option for clinical deployment. In addition, the training of the proposed model is more efficient from a memory and computational perspective, making it attractive in large-scale (e.g., 4D) settings.

Index Terms—plug and play, energy model, score model, parallel MRI

I. INTRODUCTION

The problem of reconstructing images from few of their noisy measurements is a key problem in several fields, including MRI and computer tomography. The classical approach is maximum a posteriori (MAP) estimation, which reformulates the reconstruction as an optimization problem involving a cost function that is the sum of two terms. The first term is the log-likelihood, which is a measure of data-consistency. The second one is the log-prior term that serves as a regularizer. Quadratic priors [1] as well as convex [2,3] priors are widely used in this context. Thanks to the well-defined energy, fast algorithms with theoretical convergence guarantees are available in this setting. When the regularization term is non-differentiable, these formulations rely on algorithms (e.g., FISTA [4]) that alternate between a data-consistency step and a proximal map of the prior, which can be viewed as a denoiser.

Model-based deep learning algorithms, which capitalize on the power of neural networks, were recently introduced to further improve the performance of reconstruction algorithms. For instance, the plug-and-play (PnP) methods [5]–[7] replace the

proximal map in the above algorithms by an image denoiser. By contrast, unrolled algorithms [8]–[12] unfold the iterative steps, followed by an end-to-end training of the shared DNNs, together with the data-consistency steps. The joint end-to-end training strategy offers improved performance compared to the PnP methods. However, unlike PnP methods that can be applied with arbitrary forward models, the performance of the unrolled algorithms degrades when the forward model differs from the specific training setting. Another challenge with unrolled algorithms is their large memory demand, resulting from the unrolling steps, which makes it challenging to train them for large-scale (e.g., 3D/4D) problems. Approaches to reduce the memory have been introduced [13]–[16], but they often come at the expense of increased computational complexity. By contrast, PnP models that are trained on only the image data independent of the forward model are significantly more efficient from a memory and computational complexity perspective.

Our main focus is to introduce a PnP-like framework whose performance approaches that of unrolled methods, while preserving the desirable properties of the PnP methods such as memory and computational efficiency and insensitivity to the specific forward model. We now identify some of the challenges with current PnP models that restrict their performance. Current PnP algorithms are guaranteed to converge to a fixed point, assuming the convolutional neural network (CNN) denoiser to be a contraction [16,17]. The contraction constraint is imposed by spectral normalization of the individual layers. In our experience, this assumption is highly restrictive [16] and translates to reconstruction algorithms with lower performance. The need for the above restrictive assumption is because of the lack of a well-defined energy formulation for PnP methods, which makes it challenging to adopt the well-established theoretical tools from optimization theory. An energy formulation was introduced in [18] using restrictive assumptions on the network. However, subsequent analysis showed that many of these assumptions are not satisfied by CNN-based denoisers [19].

Inspired by recent energy models [20], we model the log-prior term (regularizer) in the MAP formulation by a CNN $E_\theta(x)$. The gradient of this term $H_\theta(x) = \nabla E_\theta(x)$, which is often denoted as score function [20,21], can also be implemented as a CNN. Similar to diffusion models [20,22] and PnP methods [23], we propose to learn the score function H_θ from fully sampled images using denoising score matching (DSM) [21]. The key difference of this learning strategy from [20]–[22] is that the score network is conservative because it

The authors are with the Department of Electrical and Computer Engineering, University of Iowa, Iowa City, IA 52242 USA (e-mail: jyothi-rikhabchand@uiowa.edu; mathews-jacob@uiowa.edu).

satisfies the constraint: $\mathbf{H}_\theta = \nabla \mathbf{E}_\theta$. Thanks to the constraint, this approach also learns the energy \mathbf{E}_θ . This approach is equivalent to minimizing the Fisher divergence between the distribution modeled by \mathbf{E} and a smoothed version of the data distribution, where the smoothing is proportional to the noise standard deviation used in DSM [24]. The existence of a well-defined energy function also allows us to realize convergent image reconstruction algorithms, even when \mathbf{H}_θ is not a contraction. We introduce gradient descent and majorize-minimize algorithms with guaranteed convergence. The relaxation of the contraction constraint translates to improved performance over current PnP methods, as seen from our experiments.

The conference version of this work [25] focused on single-scale energy model and relied on gradient descent. The learned energy function \mathbf{E}_θ in our framework is not constrained as a convex function, which allows it to learn complex data distributions and thus offering improved performance. However, the use of non-convex priors can translate to convergence to local minima, especially in highly accelerated settings. To overcome this challenge, we introduce a multi-scale annealing strategy motivated by annealing strategies used in non-convex compressed sensing [26]. In particular, we learn multiple energy functions with different noise variances σ , which are used for annealed optimization. This approach, termed as Multi-Scale Energy (MuSE), improves the convergence of the algorithm to the global minimum, thus offering improved performance in challenging settings. Our experiments show that the performance of this approach is comparable to unrolled methods.

II. PROBLEM FORMULATION

Let us consider the problem of recovering an image $\mathbf{x} \in \mathbb{C}^m$ from its corrupted linear measurements $\mathbf{b} \in \mathbb{C}^n$:

$$\mathbf{A}\mathbf{x} + \mathbf{n} = \mathbf{b} \quad (1)$$

where $\mathbf{A} \in \mathbb{C}^{n \times m}$ ($n \leq m$) is a known linear transformation and $\mathbf{n} \in \mathcal{N}(0, \eta^2 \mathbf{I})$ is the additive complex white Gaussian noise. Let $p(\mathbf{x})$ be the prior of the unknown image. Then the MAP estimate of \mathbf{x} from the measurements \mathbf{b} is given by :

$$\mathbf{x}^* = \arg \max_{\mathbf{x}} \log p(\mathbf{x}|\mathbf{b}) \quad (2)$$

which simplifies to :

$$\mathbf{x}^* = \arg \min_{\mathbf{x}} \underbrace{\frac{1}{2\eta^2} \|\mathbf{A}\mathbf{x} - \mathbf{b}\|_2^2}_{-\log p(\mathbf{b}|\mathbf{x})} + \underbrace{\varphi(\mathbf{x})}_{-\log p(\mathbf{x})} \quad (3)$$

A. Plug-and-play energy models and score functions

In this paper, we model the prior $p(\mathbf{x})$ as

$$p_\theta(\mathbf{x}) = \frac{1}{\mathbf{Z}_\theta} \exp(-\mathbf{E}_\theta(\mathbf{x})). \quad (4)$$

Here, θ denotes the parameters of the model and \mathbf{Z}_θ is a normalizing constant. We model $\mathbf{E}_\theta(\mathbf{x}) : \mathbb{C}^m \rightarrow \mathbb{R}$ by a neural network. Using the above prior in (3), the MAP objective simplifies to:

$$f_{\text{MAP}}(\mathbf{x}) = \frac{1}{2\eta^2} \|\mathbf{A}\mathbf{x} - \mathbf{b}\|_2^2 + \frac{\mathbf{E}_\theta(\mathbf{x})}{\sigma^2} \quad (5)$$

Here, $\sigma^2 > 0$ is a parameter that is used in DSM as described later.

We note that the architecture of the network $\mathbf{E}_\theta : \mathbb{C}^m \rightarrow \mathbb{R}$ may be chosen in multiple ways [20]. We consider the three choices listed below, which are also shown in Figure 1.

$$\mathbf{E}_1(\mathbf{x}) = \|\mathbf{x} - \Psi_\theta(\mathbf{x})\|^2 \quad (6)$$

$$\mathbf{E}_2(\mathbf{x}) = \Phi_\theta(\mathbf{x}) \quad (7)$$

$$\mathbf{E}_3(\mathbf{x}) = \left(\frac{\|\mathbf{x}\|^2}{2} - \Phi_\theta(\mathbf{x}) \right) \quad (8)$$

Here $\Psi : \mathbb{C}^m \rightarrow \mathbb{C}^m$ and $\Phi : \mathbb{C}^m \rightarrow \mathbb{R}$ are CNN networks.

The score functions or the gradient of the energies in (6)-(8) can be computed using chain rule. For instance, we have $\nabla \mathbf{E}_1(\mathbf{x}) = \mathbf{H}_1(\mathbf{x})$, specified as:

$$\mathbf{H}_1(\mathbf{x}) = (\mathbf{x} - \Psi_\theta(\mathbf{x})) - \nabla_x \Psi_\theta(\mathbf{x} - \Psi_\theta(\mathbf{x})) \quad (9)$$

This score function and the energy function can be evaluated using a combined network as shown in Fig. 1.(a). Note that the network may be viewed to have two parts, with the second half essentially a mirror image of the first; the weights of the two halves are shared.

B. Learning the energy using denoising score matching

We first briefly discuss the DSM technique to learn the proposed energy function. We recall that the score is defined as the gradient of the log-density: $\nabla_x \log p(\mathbf{x})$. The parameters of CNN-based score models are learned and match the score of the proposed distribution $F_\theta(\mathbf{x}) = \nabla_x \log p_\theta(\mathbf{x})$, which can be viewed as the minimization of the Fisher divergence between the data and model distributions. Since the true Fisher divergence is challenging to evaluate, DSM [21] estimates the score of the smoothed distribution:

$$p_\sigma(\tilde{\mathbf{x}}) = p_{\text{data}}(\mathbf{x}) * \mathcal{N}(0, \sigma^2 \mathbf{I}). \quad (10)$$

We note that $p_\sigma(\tilde{\mathbf{x}}) \rightarrow p_{\text{data}}(\mathbf{x})$ as $\sigma \rightarrow 0$. The Fisher divergence or score-matching objective for $p_\sigma(\tilde{\mathbf{x}})$ is specified by:

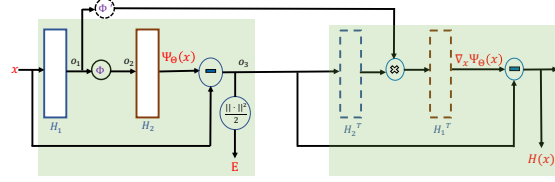
$$L_\sigma(\theta) = \mathbb{E}_{p_\sigma(\tilde{\mathbf{x}})} \|F_\theta(\tilde{\mathbf{x}}) - \nabla_{\tilde{\mathbf{x}}} \log p_\sigma(\tilde{\mathbf{x}})\|^2. \quad (11)$$

The optimization of θ using this metric is shown to be equivalent [21] to:

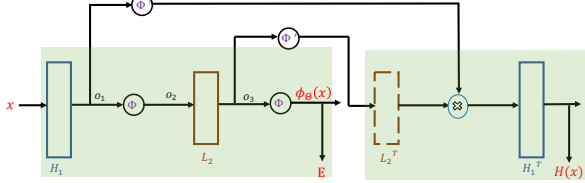
$$\begin{aligned} \theta &= \arg \min_{\theta} \mathbb{E}_{p_\sigma(\tilde{\mathbf{x}}|\mathbf{x})} \mathbb{E}_{p(\mathbf{x})} \|F_\theta(\tilde{\mathbf{x}}) - \nabla_{\tilde{\mathbf{x}}} \log p_\sigma(\tilde{\mathbf{x}}|\mathbf{x})\|^2 \\ &= \arg \min_{\theta} \mathbb{E}_{p(\mathbf{x})} \mathbb{E}_{p(z)} \left\| F_\theta(\mathbf{x} + \sigma z) + \frac{z}{\sigma} \right\|^2. \end{aligned} \quad (12)$$

In the second step, the property

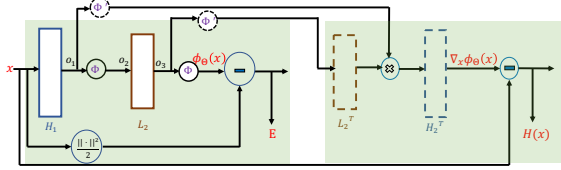
$$\nabla_{\tilde{\mathbf{x}}} \log p_\sigma(\tilde{\mathbf{x}}|\mathbf{x}) = \frac{1}{\sigma^2} (\mathbf{x} - \tilde{\mathbf{x}}) = -\frac{z}{\sigma}. \quad (13)$$



$$(a) E_1(\mathbf{x}) = \frac{1}{2} \|\mathbf{x} - \Psi_\theta(\mathbf{x})\|^2$$



$$(b) E_2(\mathbf{x}) = \Phi_\theta(\mathbf{x})$$



$$(c) E_3(\mathbf{x}) = \frac{\|\mathbf{x}\|^2}{2} - \Phi_\theta(\mathbf{x})$$

Figure 1: Illustration of a two-layer energy network to realize (a) $E_1(\mathbf{x}) = \frac{1}{2} \|\mathbf{x} - \Psi_\theta(\mathbf{x})\|^2$, (b) $E_2 = \Phi_\theta(\mathbf{x})$, and (c) $E_3(\mathbf{x}) = \frac{\|\mathbf{x}\|^2}{2} - \Phi_\theta(\mathbf{x})$. The corresponding score $H(\mathbf{x})$ is also computed using the chain rule and can be realized as a CNN.

was used. Here $p(\mathbf{z}) = \mathcal{N}(0, \mathbf{I})$. Replacing F_θ by $\nabla_{\mathbf{x}} \log(p_\theta(\mathbf{x})) = -H(\mathbf{x})/\sigma^2$, we obtain.

$$\begin{aligned} \theta &= \arg \min_{\theta} \mathbb{E}_{p_\sigma(\mathbf{z})} \left\| -\frac{H(\mathbf{x} + \sigma\mathbf{z})}{\sigma^2} + \frac{\mathbf{z}}{\sigma} \right\|^2 \\ &= \arg \min_{\theta} \mathbb{E}_{p_\sigma(\mathbf{z})} \left\| -H(\mathbf{x} + \sigma\mathbf{z}) + \underbrace{\sigma\mathbf{z}}_n \right\|^2, \end{aligned} \quad (14)$$

where $\mathbf{n} \sim \mathcal{N}(0, \sigma^2 \mathbf{I})$.

We note that DSM training is used in PnP methods and diffusion models. The main distinction of our approach from these settings is that F_θ is constrained as the gradient vector field of $\nabla_{\mathbf{x}} \log(p_\theta(\mathbf{x}))$. Constraining the score function as a conservative vector field allows us to use the fundamental theorem of line integrals [27] to represent the energy at any

given point \mathbf{x} as the line integral:

$$\log p_\theta(\mathbf{x}) = \int_C F_\theta(\mathbf{z}) d\mathbf{z} + \log p_\theta(\mathbf{a}) \quad (15)$$

where \mathbf{a} is an arbitrary point and C is any curve between \mathbf{a} and \mathbf{x} . Because the score function is conservative, the line integral in (15) is independent of the path taken. We note that this property is not valid for arbitrary residual denoisers used in classical PnP models.

We illustrate the energy learning using DSM in a toy example in Fig. 2. The results show that the energy models trained using DSM are able to learn $\nabla_{\mathbf{x}} \log p(\mathbf{x})$ as well as the associated energy. As we will see in the subsequent sections, the availability of an energy term will enable the use of fast optimization algorithms and multi-scale strategies to solve (5).

III. OPTIMIZATION ALGORITHMS

We now introduce efficient algorithms to minimize (5), where the prior term is learned using DSM as described in the earlier section. We first propose two different algorithms to minimize (5) for a fixed choice of σ . The two algorithms are based on gradient descent and majorization-minimization framework. Because the criterion in (5) is non-convex, both of these algorithms may converge to local minima. To improve the convergence to the global minimum, we introduce the multi-scale energy minimization algorithm, termed as MuSE.

A. Gradient descent algorithm

Applying gradient descent on (5), we obtain the update rule:

$$\mathbf{x}_{n+1} = \mathbf{x}_n - \gamma \left(\frac{\mathbf{A}^H(\mathbf{A}\mathbf{x}_n - \mathbf{b})}{\eta^2} + \frac{H(\mathbf{x}_n)}{\sigma^2} \right). \quad (16)$$

We assume that \mathbf{A} is normalized such that the maximum eigenvalue of $\mathbf{A}^H \mathbf{A}$ is one. We also assume that the Lipschitz constant of the score network $H(\mathbf{x})$ is upper-bounded by L , which may be greater than one. We use the CLIP approach [28] to estimate the approximate constant. Another approach may also use the product of the spectral norms of the layers of to obtain an upper-bound for L . The following result guarantees the convergence of the above algorithm to a minimum.

Lemma 3.1: The gradient descent algorithm in (16) converges to a stationary point of the MAP problem when the step size is chosen as

$$\gamma = \frac{1}{\frac{1}{\eta^2} + \frac{L}{\sigma^2}} \quad (17)$$

Please see Appendix A for proof. We note that the above result does not require H to be a contraction, unlike prior PnP approaches [29,30]. The result is a consequence of the existence of a valid energy E . We denote the PnP energy approach solved using the gradient-descent algorithm by EPnP-GD.

B. Majorization-minimization (MM) algorithm

The MM framework minimizes the problem (5) iteratively, wherein at every iteration a surrogate function $g(\mathbf{x}|\mathbf{x}_n)$ is minimized to get the next iterate. To construct a surrogate function for the cost function in (5), we use the following proposition. [31].

Proposition 3.1: Let $\mathbf{E}(\mathbf{x})$ be a continuously differentiable function with a Lipschitz constant L . Then, $\mathbf{E}(\mathbf{x})$ can be majorized by the quadratic function:

$$E(\mathbf{x}) \leq E(\mathbf{x}_n) + \text{Re}(\mathbf{H}(\mathbf{x}_n)^H(\mathbf{x} - \mathbf{x}_n)) + \frac{L}{2}\|\mathbf{x} - \mathbf{x}_n\|^2 \quad (18)$$

Please see lemma 8.1 under Appendix A for proof. The above relation can be used to majorize (5) as $f_{\text{MAP}}(\mathbf{x}) \leq g(\mathbf{x}|\mathbf{x}_n)$, where

$$g(\mathbf{x}|\mathbf{x}_n) = \frac{\|\mathbf{A}\mathbf{x} - \mathbf{b}\|^2}{2\eta^2} + \frac{\mathbf{E}_\theta(\mathbf{x}_n)}{\sigma^2} + \frac{L}{2\sigma^2}\|\mathbf{x} - \mathbf{x}_n\|^2 + \frac{\text{Re}(\mathbf{H}_\theta(\mathbf{x}_n)^H(\mathbf{x} - \mathbf{x}_n))}{\sigma^2} \quad (19)$$

The above quadratic cost function can be solved to obtain the MM update rule:

$$\mathbf{x}_{n+1} = \arg \min_{\mathbf{x}} g(\mathbf{x}|\mathbf{x}_n) \quad (20)$$

The analytical solution of (20) is specified by

$$\mathbf{x}_{n+1} = \left(\frac{\mathbf{A}^H \mathbf{A}}{\eta^2} + \frac{L}{\sigma^2} \mathbf{I} \right)^{-1} \left(\frac{\mathbf{A}^H \mathbf{b}}{\eta^2} + \frac{L\mathbf{x}_n - \mathbf{H}_\theta(\mathbf{x}_n)}{\sigma^2} \right) \quad (21)$$

We propose to solve the above equation using the conjugate gradients algorithm. Thanks to the constraint $\nabla \mathbf{E} = \mathbf{H}$, the MM algorithm is guaranteed to converge as shown below, even when \mathbf{H} is not a contraction.

Proposition 3.2: The sequence $\{\mathbf{x}_n\}$ generated by the MM algorithm will monotonically decrease the cost function and will converge to a stationary point of (5).

The proof for this Lemma is given in Appendix B. We note that when $\frac{L}{\sigma^2} \gg \frac{1}{\eta^2}$ (e.g., large Lipschitz constant or high measurement noise variance denoted by η), we have $(\mathbf{A}^H \mathbf{A} / \eta^2 + L / \sigma^2 \mathbf{I}) \approx (L / \sigma^2 \mathbf{I})$. In this case, the MM algorithm simplifies to the gradient descent. Specifically, the surrogate function defined in (19) will be a looser bound and hence both gradient descent and the MM algorithm will have a similar convergence rate. Hence, for such cases, to save computation time, we switch to gradient descent. By contrast, the MM algorithm offers faster convergence when $\frac{L}{\sigma^2} < \frac{1}{\eta^2}$. We denote the PnP energy approach, solved using the MM algorithm, by EPnP-MM.

C. Multi-Scale Energy (MuSE) algorithm

We note that the learned energy function \mathbf{E} and, hence, the cost function (5) are not constrained to be convex functions. Hence, the above algorithms are only guaranteed to converge to a local minimum, which may not be the desired one. Inspired by continuation strategies used in non-convex optimization algorithms, we introduce a similar strategy to

improve the convergence to the global minimum. In particular, we consider a sequence of energies, which are smooth approximations of the true energy, parameterized by the scale parameter σ . We start with a coarse scale and gradually reduce the scale. For each scale parameter, the solution is obtained as the minimum of the energy function at that scale using the above described algorithms. The solution at a specific scale is used as the initialization for the algorithm at the next finer scale. We gradually reduce the scale parameter. We term this multi-scale algorithm as MuSE.

To realize MuSE, we first learn $p_\sigma(\mathbf{x})$ as defined in (10) for various values of σ . For large values of sigma, $p_\sigma(\mathbf{x})$ will be a smooth approximation of $p_\theta(\mathbf{x})$ and for $\sigma \rightarrow 0$, $p_\sigma(\mathbf{x}) \approx p_\theta(\mathbf{x})$. See Fig. 2 for an illustration. Similarly, we also consider smoother approximations of the likelihood term in (5) by varying η^2 . Each of the smoothed energy functions are learned using (14). The pseudocode of MuSE is shown in Table 3.

IV. ILLUSTRATION OF ENERGY LEARNING

We demonstrate the DSM learning of a simple dataset that facilitates the visualization of the learned energies. We consider a Gaussian mixture dataset with four clusters. We consider three different scale parameters $\sigma = \{0.5, 0.2, 0.1\}$ to illustrate the annealing process. Fig. 2.(a)-Fig. 2.(c) shows the iso-contours of $\frac{\mathbf{E}_1}{\sigma^2}$ (where \mathbf{E}_1 is specified as in (6)) as well as the arrows indicating $\frac{\mathbf{H}_1}{\sigma^2}$. Red dots in the figure indicate the samples of the Gaussian mixture model. The function $\Psi_\theta(\mathbf{x})$ in (6) was constructed using a four-layer linear network with 128 channels per layer and 3×3 filters. After each linear layer, the rectified linear unit (ReLU) activation function is used, except for the last layer. To show the benefits of using multiple noise levels, different score functions \mathbf{H}_{σ_i} are trained. We also train different score functions that are not conservative functions, which are used in traditional PnP formulations. We consider two settings: score functions without contraction constraint in Fig. 2.(d)-Fig. 2.(f) and with contraction constraint with spectral normalization in Fig. 2.(g)-Fig. 2.(i). Note that contraction constraints are needed for traditional PnP algorithms to converge, while MuSE algorithms do not require them.

We note from Fig. 2.(c) and Fig. 2.(f) that the energy model and the unconstrained score model can provide good estimates of score for small values of σ . In particular, the arrows point to the means of the Gaussians. We also note from Fig. 2.(a) and Fig. 2.(b) that as the scale parameter σ increases, the energy representations are simple with a well-defined minimum. The multi-scale learning approach that learns a sequence of coarse to fine energies is expected to improve the convergence of the algorithms in the context of inverse problems. We note from Fig. 2.(h) & Fig. 2.(i) that the addition of the spectral normalization constraint severely restricts the network from learning score. In particular, the arrows do not point to the red dots. The use of such a constrained model may thus fail

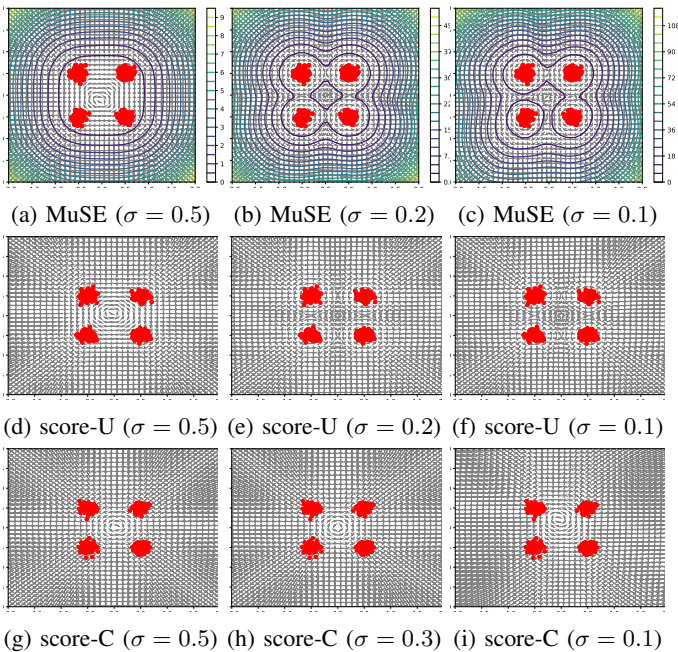


Figure 2: Rows 1 - 3: Illustration of MuSE, Annealed Score Model, and Annealed Contraction Score Model for Gaussian mixture data set.

to capture the properties of a complex data distribution, thus restricting performance in inverse problems.

V. PARALLEL MRI EXPERIMENTS AND RESULTS

A. Data set

The performance of the proposed method is evaluated in the context of reconstructing MR images from its undersampled measurements. In this case, the linear operator \mathbf{A} in (1) is $\mathbf{A} = \mathbf{SFC}$, where \mathbf{S} is the sampling matrix, \mathbf{F} is the Fourier transform, and \mathbf{C} is the coil sensitivity map. The experiments are conducted on the multi-channel knee MRI data sets from the fast MRI challenge [32]. In particular, it is a 15 coil knee data set and consists of complex images of matrix size 320×320 . The training, validation, and test set consists of data from 45, 5, and 50 subjects, respectively. The models are evaluated for two-fold and four-fold retrospectively undersampled measurements, which are obtained by sampling the data along the phase-encoding direction using a 1D non-uniform variable-density mask.

B. Architecture of the networks

The function $\Psi_\theta(\mathbf{x})$ when $E(\mathbf{x}) = \Psi_\theta(\mathbf{x})$, and $E(\mathbf{x}) = \frac{\|\mathbf{x}\|^2}{2} - \Psi_\theta(\mathbf{x})$ is implemented using a five-layer convolutional layer followed by a linear layer. The convolutional layer consists of 64 channels per layer and 3×3 filter. After each convolutional layer, the ReLU activation function is used. The function $\Psi_\theta(\mathbf{x})$ when $E(\mathbf{x}) = \frac{1}{2}\|\mathbf{x} - \Psi_\theta(\mathbf{x})\|^2$ also follows a similar architecture; however it does not require an additional linear layer at the end. Score $\mathbf{H}(\mathbf{x})$ for each energy function is implemented using the chain rule as discussed earlier in Section II. This ensures that the computed score is a

conservative function. We also implement a non-conservative score model with a ten-layer CNN with 64 channels with ReLU activations. The contraction constraint was imposed using spectral normalization [33]. All the models were trained using DSM. We first compare the performance of the energy models with score models with and without the contraction constraint in the context of image denoising.

Pseudocode of MuSE

Inputs: Forward operator: \mathbf{A} , Scale parameters: $\{(\eta_1^2, \sigma_1^2); \dots; (\eta_k^2, \sigma_k^2)\}$, Pre-trained denoisers: $\{H_{\sigma_1}(\mathbf{x}_n), \dots, H_{\sigma_k}(\mathbf{x}_n)\}$

Initialize: Set $(n, k) = 0$, Initialize $\tilde{\mathbf{x}}_0$ and \mathbf{x}_0 .

Repeat: Given $\tilde{\mathbf{x}}_k$ perform the $k + 1$ -th step.

$n \leftarrow 0$

Repeat: Given \mathbf{x}_n perform the $n + 1$ -th step.

Compute \mathbf{x}_{n+1} either using (16) or (21), $n \leftarrow n + 1$

until convergence

$\tilde{\mathbf{x}}_k = \mathbf{x}_{n+1}$, $k \leftarrow k + 1$, **until convergence**

Output: $\mathbf{x}_{\text{MuSE}}^* = \tilde{\mathbf{x}}_k$

C. Denoising performance of energy model $E(\mathbf{x})$

Before comparing the performance of the models in the context of image reconstruction, we evaluate the three energy models and traditional score models with and without contraction constraint in the context of denoising. We consider two different scale factors $\sigma = 0.01$ and $\sigma = 0.05$. The trained score models are evaluated on the validation data set. Table I compares the denoising performance. From the table, we observe that $E_1(\mathbf{x}) = \frac{1}{2}\|\mathbf{x} - \Psi_\theta(\mathbf{x})\|^2$ offers the highest average PSNR when compared to other energy models, which is consistent with [20]. We also note that the score model trained without any constraints offers marginally higher performance than $E_1(\mathbf{x})$, while the score model with contraction constraint offers poor performance. Note that the contraction constraint is needed for PnP models that use traditional score models to converge. We show the noisy and denoised images in Fig. 3. Because $E_1(\mathbf{x})$ offers improved denoising, we use this energy model for the remaining studies.

Table I: Denoising performance of energy and score models

Energy Model	PSNR $\sigma = 0.01$	PSNR $\sigma = 0.05$
$E_1(\mathbf{x}) = \frac{1}{2}\ \mathbf{x} - \psi_\theta(\mathbf{x})\ ^2$	42.18 ± 3.9	34.71 ± 3.25
$E_2(\mathbf{x}) = \psi_\theta(\mathbf{x})$	40.5 ± 3.71	30.95 ± 3.82
$E_3(\mathbf{x}) = \frac{\ \mathbf{x}\ ^2}{2} - \psi_\theta(\mathbf{x})$	33.23 ± 3.61	29.97 ± 2.78
Score-C	36.54 ± 4.98	22.43 ± 5.01
Score-U	42.71 ± 4.01	34.38 ± 2.98

D. Comparison E -PnP-GD and E -PnP-MM algorithms.

In this section, we compare the convergence rates of the gradient descent and MM algorithms described in Sections III-A and III-B, respectively. The denoiser $H(\mathbf{x})$ used in both the algorithms were trained to be a noise estimator for $\sigma = 0.07$. The algorithms were made to run until $|f_{\text{MAP}}(\mathbf{x}_{n+1}) -$

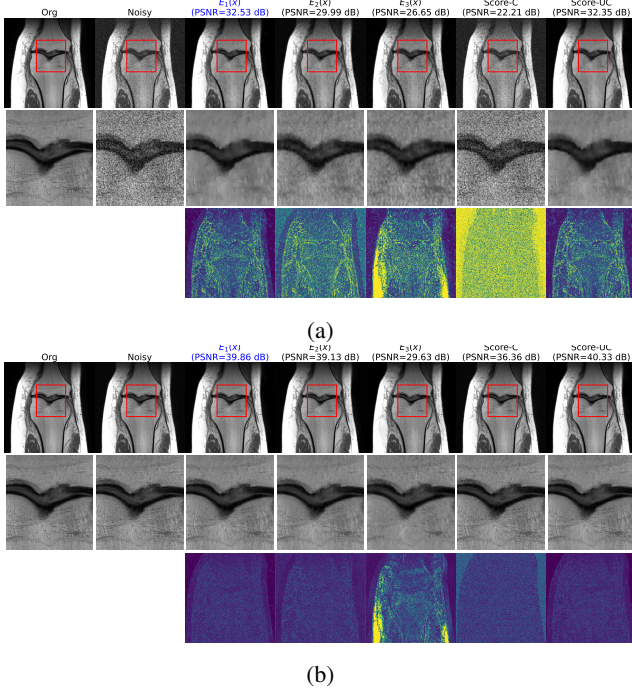


Figure 3: Denoising performance of the different energy models and score networks, when the MR images are corrupted with Gaussian noise for (a) $\sigma = 0.05$ and (b) $\sigma = 0.01$. For each of the settings, the first row compares the denoised images, the second row shows the zoomed section of the images, and the third row shows the corresponding error images. The error images are scaled in magnitude by a factor of 10 for improved visualization.

$f_{\text{MAP}}(\mathbf{x}_{n+1}) \leq |f_{\text{MAP}}(\mathbf{x}_n)| \cdot \epsilon$, where the threshold ϵ was set to 10^{-5} . To have a fair comparison, both the algorithms were initialized with the same initial value $\mathbf{A}^H \mathbf{b}$. We consider two different values of η^2/σ^2 in Fig. 4.(a) and Fig. 4.(b), where η is the noise variance of the measurements and σ is the scale at which the energy is learned. In the low-noise case, the data-term is weighted higher; MM offers a faster convergence in this setting. By contrast, in the higher noise setting (higher η), the weight of the data term is lower and hence the MM does not offer a significant improvement over gradient descent.

E. Comparison of MuSE with EPnP-GD and EPnP-MM

In this section, we show the benefit of using multiple noise scales to reconstruct the MRI images. In this regard, we use seven noise scales $\eta = \sigma = \{0.09, 0.07, 0.05, 0.03, 0.01, 0.005, 0.001\}$ and train separate denoisers $H_{\sigma_i}(\mathbf{x})$. Then, using the trained denoiser, we implement MuSE as discussed in Section III.C. The sub-problem $f_{\text{MAP}}^i(\mathbf{x})$ corresponding to the i -th noise level is run until a threshold ϵ_i is reached. We set ϵ_i according to the following schedule: $\{10^{-5}, 10^{-5}, 10^{-4}, 10^{-4}, 10^{-4}, 10^{-3}, 10^{-3}\}$. The threshold and noise levels were chosen based on the performance of the validation data set. We also implement EPnP-GD and EPnP-MM, which use a single noise scale: $\sigma = 10^{-3}$, which was the final noise scale used in MuSE. The algorithms

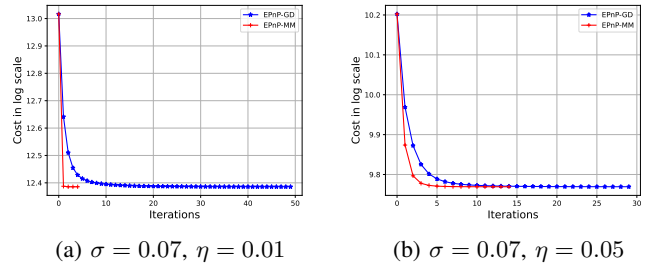


Figure 4: Convergence plot of EPnP-GD and EPnP-MM for two different scale parameters σ and measurement noise values η . (a) shows a low noise setting, where the data term is weighted higher (small value of $L\eta^2/\sigma^2$), while (b) is a higher noise setting. It is observed that MM is beneficial when $L\eta^2/\sigma^2$, because the data term has a higher weight in this setting.

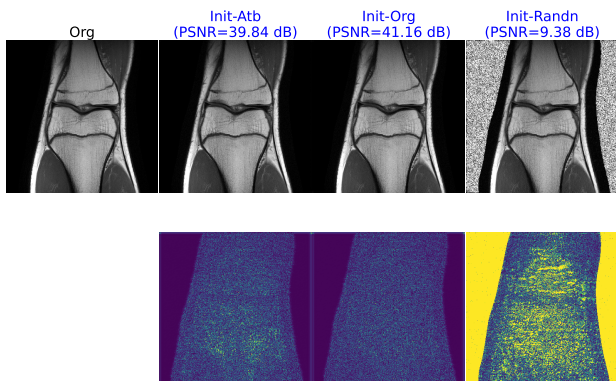
are tested on a two-fold data set. To study the convergence of the algorithms to local minima, we test them with three different initializations: (a) $\mathbf{A}^H \mathbf{b}$, (b) randomly from a zero-mean complex Gaussian distribution with unit variance, and (c) original image \mathbf{x} .

Fig. 5.a, Fig. 5.b, and Fig. 5.c compare EPnP-GD, EPnP-MM, and MuSE reconstructions for a two-fold acceleration setting. We observe that MuSE performs consistently well for all the initializations and offers the best PSNR of 41.51 dB when compared to EPnP-MM and EPnP-GD, which offers the highest PSNRs of 41.13 dB and 41.16 dB, respectively. We also show the convergence plot of MuSE in Fig. 5.d, which shows that MuSE converges to similar solutions for the three different initializations.

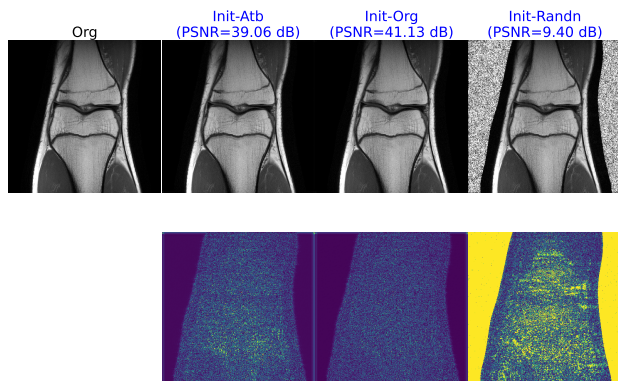
F. Application to MRI reconstruction

In this section, we compare the proposed energy-based algorithms MuSE, EPnP-MM, and EPnP-GD against unrolled MODL [11] and PnP ISTA [17] in the context of accelerated MRI. The inference standard deviation η and score standard deviation σ for MuSE, EPnP-MM, and EPnP-GD are kept the same as in the previous experiment. PnP-ISTA is implemented with 500 iterations. Note that unlike the energy models, the score network of PnP-ISTA requires that the Lipschitz constant of the network be bounded by one. The algorithms are compared for both two-fold and four-fold accelerations.

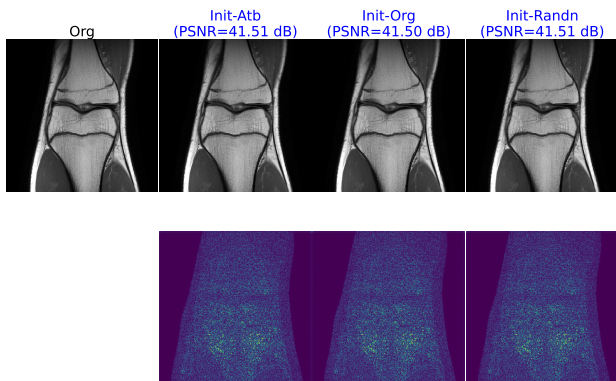
Table II shows the result of the algorithms for both accelerations. Fig. 6a and Fig. 6b show the reconstructed images for two-fold and four-fold acceleration, respectively. From the table, we observe that MuSE and E2E-MODL results offer comparable PSNR values. We also see from Fig. 6a and Fig. 6b that the image quality of these algorithms is comparable. We note that the E2E-MoDL uses end-to-end training and hence requires 10-fold more memory and computational complexity than MuSE during training. We note that the EPnP-MM and EPnP-GD methods offer lower PSNR values and alias artifacts compared to MuSE and MoDL, especially at the four-fold



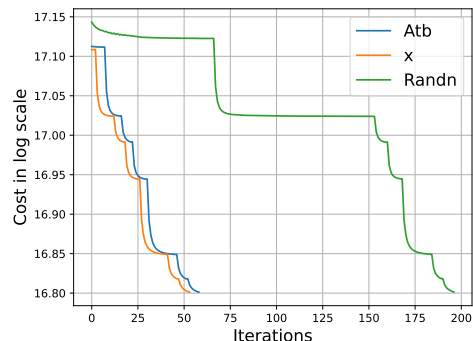
(a) EPnP-GD reconstructions for different initializations



(b) EPnP-MM reconstructions for different initializations



(c) MuSE reconstructions for different initializations



(d) Convergence of MuSE for different initializations

Figure 5: Comparison of convergence of EPnP-GD, EPnP-MM, and MuSE for different initializations. Sub-figures (a),(b),(c): Top row compares the reconstructed images, while the bottom row shows the corresponding error images. We note that the MUSE algorithm with $A^H b$ initialization converges in 50 iterations, while the one using random initialization converges in around 200 iterations. However, all of the algorithms converge to the same solution, as seen from the comparable PSNR and energy values. By contrast, EPnP-GD and EPnP-MM converge to different solutions depending on the initialization.

acceleration setting. The denoiser in PnP-ISTA is trained with spectral normalization, which constrains the network, resulting in lower performance.

We note that E2E-MODL, which relies on end-to-end training, is ideally suited when the A operator is matched. However, the performance of the trained model degrades significantly when used with a different A operator, as shown in Table III. In particular, we use the MODL network trained on two-fold undersampling on four-fold data, which results in a 3 dB drop in the performance compared to MuSE. The ability of MuSE to be used with arbitrary forward models makes it attractive compared to unrolled algorithms that need to be trained for different settings.

Table III: Generalization performance of MuSE

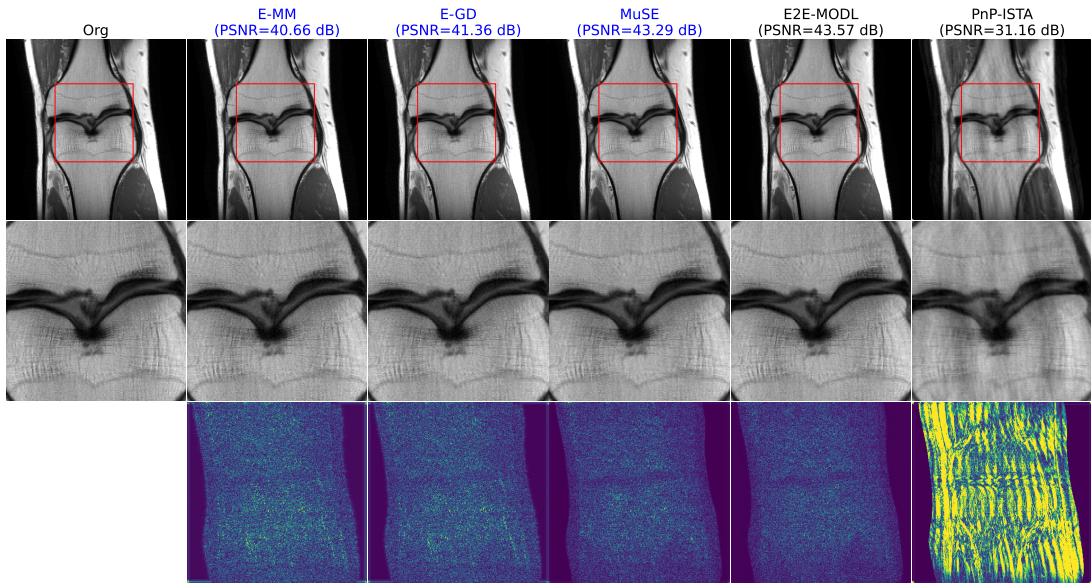
Algorithm	PSNR \pm std
MuSE	38.07 \pm 3.84
E2E-MODL(trained on two-fold)	36.87 \pm 3.97

Table II: Comparison of the models in the context of accelerated MRI at two different accelerations.

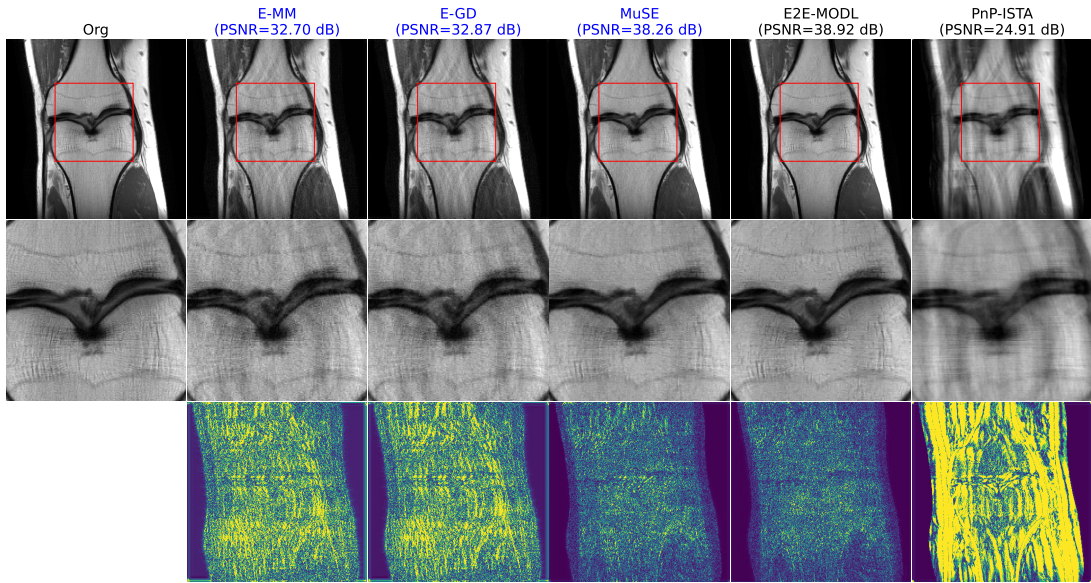
Algorithm	Avg. PSNR \pm std	
	Acceleration 2x	Acceleration 4x
MuSE	44.04 \pm 4.03	38.07 \pm 3.84
EPnP-GD	41.98 \pm 4.15	34.21 \pm 4.18
EPnP-MM	41.48 \pm 4.01	33.85 \pm 4.18
E2E-MODL	44.72 \pm 3.89	39.42 \pm 3.54
PnP-ISTA	32.87 \pm 3.24	27.35 \pm 3.45

VI. DISCUSSION

The results in Figure 3 show that the denoising performance of the energy model E_1 is comparable to the unconstrained score model. However, the score model with the contraction constraint translates to lower performance. The proposed gradient descent and MM algorithms can converge, even when H is not constrained to be a contraction. This translates to the improved performance of the EPnP-MM and EPnP-GD algorithms over PnP-ISTA in Fig. 6a and Fig. 6b. Note that PnP-ISTA requires the score network to be a contraction.



(a) Two-fold acceleration



(b) Four-fold acceleration

Figure 6: Example reconstruction using MuSE, EPnP-GD, EPnP-MM, PnP-ISTA, and MODL at two different accelerations on fast-MRI data. The MoDL algorithm was trained for each acceleration setting separately. By contrast, we used the same energy and score networks for both settings. (a) Results at two-fold acceleration using Cartesian undersampling pattern. (b) Results at two-fold acceleration using Cartesian undersampling pattern. The top rows of each plot show the reconstructed images, while the second rows show the enlarged image. The third rows correspond to the error images, which are scaled by a factor of 10 to highlight the differences.

The experiments in Fig. 5 show the benefit of the multi-scale strategy. In particular, the GD and MM algorithm is observed to converge to different solutions, as seen in Fig. 5.(a) and Fig. 5.(b). By contrast, the multi-scale strategy improves the convergence, yielding the same solution irrespective of the initialization. From Figures 5c and 5a, we observe a 1.5 dB increase in PSNR with the multi-scale strategy when the initialization is $A^H b$. The improved performance offered by the relaxation of the contraction constraint and the multi-scale

strategy brings the performance of the proposed scheme closer to that of the unrolled MoDL approach that is trained in an end-to-end fashion, as seen in Table III.

The performance of the proposed scheme comes at the expense of a larger number of iterations (e.g., 50-100 iterations as seen in Fig. 5d) with $A^H b$ initialization compared to unrolled algorithms (e.g., 10 iterations in MoDL); inference is 5-10 times slower. However, the energy formulation in MuSE enables the use of sophisticated algorithms from the

optimization literature to this setting to further reduce the run time. However, these extensions are beyond the scope of the current work. We also note that the proposed scheme is significantly more computational and memory efficient during training when compared to unrolled algorithms. This approach may thus be beneficial in large-scale (e.g., 4D) problems, where unrolled algorithms are infeasible. We plan to explore these applications in our future work. Another benefit of the proposed scheme is its ability to be used in arbitrary inverse problems as seen in Table III. By contrast, the performance of unrolled algorithms degrades when the forward model differs from the training setting.

We currently have trained the energy model for a single contrast. However, the approach can be generalized to multiple contrasts, field strengths, or anatomies as in [34,35]. On a similar note, the proposed score/energy model may also be used with Langevin dynamics for reconstruction and to derive uncertainty maps as in [36]–[38].

VII. CONCLUSION

We introduced a novel plug-and-play energy formulation for inverse problems. The proposed framework models the log-prior of the data using a deep CNN. The gradient of the log-prior yields the score function, which is learned using denoising score matching. We introduced the steepest descent and majorize-minimize algorithms, which are guaranteed to converge to a minimum of the resulting MAP objective, even when the score function is not a contraction. Our experiments show that the elimination of the contraction constraint translates to improved performance. We also introduce a multi-scale optimization strategy termed as MuSE to improve the convergence of the algorithm to the global minimum of the MAP objective. The preliminary results in the context of MRI show that the multi-scale energy framework offers performance comparable to that of unrolled algorithms, while being generalizable to arbitrary forward models.

VIII. APPENDIX A: PROOF OF LEMMA 3.1

We first state the result that a Lipschitz-bounded function can be upper-bounded by a quadratic function [39].

Lemma 8.1: Let f be a continuously differentiable function with Lipschitz constant L i.e.,

$$\|\nabla f(\mathbf{y}) - \nabla f(\mathbf{x})\| \leq L\|\mathbf{y} - \mathbf{x}\| \quad \forall \mathbf{x}, \mathbf{y} \in \text{dom } f. \quad (22)$$

If $\text{dom } f$ is convex, then the following inequality holds:

$$f(\mathbf{x}) \leq f(\mathbf{y}) + \text{Re}(\nabla f(\mathbf{y})^H(\mathbf{x} - \mathbf{y})) + \frac{L}{2}\|\mathbf{x} - \mathbf{y}\|^2 \quad (23)$$

Proof: The short proof is provided to make the paper self contained. From (22) we get:

$$\|\nabla f(\mathbf{y}) - \nabla f(\mathbf{x})\| \|\mathbf{y} - \mathbf{x}\| \leq L\|\mathbf{y} - \mathbf{x}\|^2 \quad (24)$$

Then by Cauchy-Schwartz inequality, we have

$$\begin{aligned} \text{Re}((\nabla f(\mathbf{y}) - \nabla f(\mathbf{x}))^H(\mathbf{y} - \mathbf{x})) &\leq \|\nabla f(\mathbf{y}) - \nabla f(\mathbf{x})\| \|\mathbf{y} - \mathbf{x}\| \\ &\leq L\|\mathbf{y} - \mathbf{x}\|^2 \end{aligned} \quad (25)$$

Let us consider $\mathbf{x}, \mathbf{y} \in \text{dom } f$ and let $u(t) = f(\mathbf{y} + t(\mathbf{x} - \mathbf{y}))$. Note that $u(t)$ is defined for $t \in [0, 1]$ since the domain of f is convex. We have

$$u'(t) = \text{Re}(\nabla f(\mathbf{y} + t(\mathbf{x} - \mathbf{y}))^H(\mathbf{x} - \mathbf{y})).$$

Then we have:

$$\begin{aligned} u'(t) - u'(0) &= \text{Re}((\nabla f(\mathbf{y} + t(\mathbf{x} - \mathbf{y})) - \nabla f(\mathbf{y}))^H(\mathbf{x} - \mathbf{y})) \\ &\leq tL\|\mathbf{y} - \mathbf{x}\|^2 \end{aligned}$$

where the last inequality is by (25). Then,

$$\begin{aligned} f(\mathbf{x}) &= u(1) = u(0) + \int_0^1 u'(t) dt \\ &\leq u(0) + \int_0^1 (Lt\|\mathbf{y} - \mathbf{x}\|^2 + u'(0)) dt \\ &= f(\mathbf{y}) + \frac{L}{2}\|\mathbf{y} - \mathbf{x}\|^2 + \text{Re}(\nabla f(\mathbf{y})^H(\mathbf{x} - \mathbf{y})) \end{aligned}$$

■

A. Proof of Lemma 3.1

Proof: The gradient of the cost function $f_{\text{MAP}}(\mathbf{x})$ is Lipschitz continuous with constant $\tilde{L} = \frac{1}{\eta^2} + \frac{L}{\sigma^2}$. Then applying Lemma 8.1, we obtain

$$f_{\text{MAP}}(\mathbf{x}) \leq f_{\text{MAP}}(\mathbf{x}_n) + \text{Re}(\nabla f_{\text{MAP}}(\mathbf{x}_n)^H(\mathbf{x} - \mathbf{x}_n)) + \frac{\tilde{L}}{2}\|\mathbf{x} - \mathbf{x}_n\|^2 \quad (26)$$

We now consider the gradient descent update $\mathbf{x}_{n+1} = \mathbf{x}_n - \gamma \nabla f_{\text{MAP}}(\mathbf{x}_n)$ and evaluate the cost at \mathbf{x}_{n+1} :

$$\begin{aligned} f_{\text{MAP}}(\mathbf{x}_{n+1}) &\leq f_{\text{MAP}}(\mathbf{x}_n) - \gamma \|\nabla f_{\text{MAP}}(\mathbf{x}_n)\|^2 \\ &\quad + \frac{\tilde{L}}{2}\gamma^2 \|\nabla f_{\text{MAP}}(\mathbf{x}_n)\|^2 \\ &= f_{\text{MAP}}(\mathbf{x}_n) - (1 - \frac{\tilde{L}}{2}\gamma)\gamma \|\nabla f_{\text{MAP}}(\mathbf{x}_n)\|^2 \end{aligned}$$

When $\gamma \leq \frac{1}{\tilde{L}}$, we have $-(1 - \frac{\tilde{L}}{2}\gamma)\gamma = \frac{\tilde{L}}{2}\gamma - 1 \leq -\frac{1}{2}$. Therefore, the above inequality becomes:

$$f_{\text{MAP}}(\mathbf{x}_{n+1}) \leq f_{\text{MAP}}(\mathbf{x}_n) - \frac{\gamma}{2} \|\nabla f_{\text{MAP}}(\mathbf{x}_n)\|^2 \quad (27)$$

Note that for $\mathbf{x} \neq \mathbf{x}^*$, $\frac{\gamma}{2} \|\nabla f_{\text{MAP}}(\mathbf{x})\|^2 > 0$. This implies that gradient descent will decrease the cost function at every iteration until it reaches $\mathbf{x} = \mathbf{x}^*$, for which $\nabla f_{\text{MAP}}(\mathbf{x}^*) = 0$. ■

IX. APPENDIX B: PROOF OF LEMMA 3.2

Note that the surrogate function $g(\mathbf{x}|\mathbf{x}_n)$ defined in (19) satisfies the following inequalities:

$$g(\mathbf{x}|\mathbf{x}_n) \geq f_{\text{MAP}}(\mathbf{x}_n) \quad (28)$$

$$g(\mathbf{x}_n|\mathbf{x}_n) = f_{\text{MAP}}(\mathbf{x}_n) \quad (29)$$

Using the above inequality we get:

$$f_{\text{MAP}}(\mathbf{x}_{n+1}) \leq g(\mathbf{x}_{n+1}|\mathbf{x}_n) \leq g(\mathbf{x}_n|\mathbf{x}_n) = f_{\text{MAP}}(\mathbf{x}_n). \quad (30)$$

The second inequality is true because \mathbf{x}_{n+1} is the minimum of the surrogate function in (20). Therefore, from (30) it is easy to see that the sequence of iterates $\{\mathbf{x}_n\}$ generated by the EPnP-MM algorithm will decrease the cost function monotonically:

$$f_{\text{MAP}}(\mathbf{x}_0) \geq f_{\text{MAP}}(\mathbf{x}_1) \geq f_{\text{MAP}}(\mathbf{x}_2) \geq \dots \quad (31)$$

Let \mathbf{z} be the limit point of $\{\mathbf{x}_n\}$ and let $\{\mathbf{x}_{r_n}\}$ be a subsequence of $\{\mathbf{x}_n\}$ converging to a limit point \mathbf{z} . Then from (28), (29) and (31), we have:

$$\begin{aligned} g(\mathbf{x}_{r_{n+1}}|\mathbf{x}_{r_{n+1}}) &= f(\mathbf{x}_{r_{n+1}}) \leq f(\mathbf{x}_{r_n+1}) \leq g(\mathbf{x}_{r_n+1}|\mathbf{x}_{r_n}) \\ &\leq g(\mathbf{x}|\mathbf{x}_{r_n}) \end{aligned} \quad (32)$$

Letting $n \rightarrow \infty$, we get

$$g(\mathbf{z}|\mathbf{z}) \leq g(\mathbf{x}|\mathbf{z}) \quad (33)$$

which implies $g'(\mathbf{z}|\mathbf{z}) = 0$, where $g'(\mathbf{z}|\mathbf{z})$ is the derivative of the surrogate function at point \mathbf{z} . Then by Proposition 1 in [40], the surrogate function and the objective function will have the same first-order behavior at \mathbf{z} . Therefore, $g'(\mathbf{z}|\mathbf{z}) = 0$ implies that $f'(\mathbf{z}) = 0$. Hence, \mathbf{z} is a stationary point of problem (5).

REFERENCES

- [1] A. N. Tikhonov and V. I. Arsenin, *Solutions of Ill-posed Problems: Andrey N. Tikhonov and Vasilii Y. Arsenin. Translation Editor Fritz John*. Wiley, 1977.
- [2] D. L. Donoho, "Compressed sensing," *IEEE Transactions on information theory*, vol. 52, no. 4, pp. 1289–1306, 2006.
- [3] E. J. Candès, J. Romberg, and T. Tao, "Robust uncertainty principles: Exact signal reconstruction from highly incomplete frequency information," *IEEE Transactions on information theory*, vol. 52, no. 2, pp. 489–509, 2006.
- [4] A. Beck and M. Teboulle, "A fast iterative shrinkage-thresholding algorithm for linear inverse problems," *SIAM journal on imaging sciences*, vol. 2, no. 1, pp. 183–202, 2009.
- [5] S. V. Venkatakrisnan, C. A. Bouman, and B. Wohlberg, "Plug-and-play priors for model based reconstruction," in *2013 IEEE Global Conference on Signal and Information Processing*, 2013, pp. 945–948.
- [6] G. T. Buzzard, S. H. Chan, S. Sreehari *et al.*, "Plug-and-play unplugged: Optimization-free reconstruction using consensus equilibrium," *SIAM Journal on Imaging Sciences*, vol. 11, no. 3, pp. 2001–2020, 2018.
- [7] R. Ahmad, C. A. Bouman, G. T. Buzzard *et al.*, "Plug-and-play methods for magnetic resonance imaging: Using denoisers for image recovery," *IEEE signal processing magazine*, vol. 37, no. 1, pp. 105–116, 2020.
- [8] V. Monga, Y. Li, and Y. C. Eldar, "Algorithm unrolling: Interpretable, efficient deep learning for signal and image processing," *IEEE Signal Processing Magazine*, vol. 38, no. 2, pp. 18–44, 2021.
- [9] J. Sun, H. Li, Z. Xu *et al.*, "Deep admm-net for compressive sensing mri," *Advances in neural information processing systems*, vol. 29, 2016.
- [10] K. Hammernik, T. Klatzer, E. Kobler *et al.*, "Learning a variational network for reconstruction of accelerated mri data," *Magnetic resonance in medicine*, vol. 79, no. 6, pp. 3055–3071, 2018.
- [11] H. K. Aggarwal, M. P. Mani, and M. Jacob, "Modl: Model-based deep learning architecture for inverse problems," *IEEE transactions on medical imaging*, vol. 38, no. 2, pp. 394–405, 2018.
- [12] T. Küstner, N. Fuin, K. Hammernik *et al.*, "Cinenet: deep learning-based 3d cardiac cine mri reconstruction with multi-coil complex-valued 4d spatio-temporal convolutions," *Scientific reports*, vol. 10, no. 1, p. 13710, 2020.
- [13] S. Bai, J. Z. Kolter, and V. Koltun, "Deep equilibrium models," *Advances in Neural Information Processing Systems*, vol. 32, 2019.
- [14] M. Kellman, K. Zhang, E. Markley *et al.*, "Memory-efficient learning for large-scale computational imaging," *IEEE Transactions on Computational Imaging*, vol. 6, pp. 1403–1414, 2020.
- [15] D. Gilton, G. Ongie, and R. Willett, "Deep equilibrium architectures for inverse problems in imaging," *IEEE Transactions on Computational Imaging*, vol. 7, pp. 1123–1133, 2021.
- [16] A. Pramanik, M. B. Zimmerman, and M. Jacob, "Memory-efficient model-based deep learning with convergence and robustness guarantees," *IEEE Transactions on Computational Imaging*, vol. 9, pp. 260–275, 2023.
- [17] E. Ryu, J. Liu, S. Wang *et al.*, "Plug-and-play methods provably converge with properly trained denoisers," in *International Conference on Machine Learning*. PMLR, 2019, pp. 5546–5557.
- [18] Y. Romano, M. Elad, and P. Milanfar, "The little engine that could: Regularization by denoising (red)," *SIAM Journal on Imaging Sciences*, vol. 10, no. 4, pp. 1804–1844, 2017.
- [19] E. T. Reehorst and P. Schniter, "Regularization by denoising: Clarifications and new interpretations," *IEEE transactions on computational imaging*, vol. 5, no. 1, pp. 52–67, 2018.
- [20] T. Salimans and J. Ho, "Should ebms model the energy or the score?" in *Energy Based Models Workshop-ICLR 2021*, 2021.
- [21] P. Vincent, "A connection between score matching and denoising autoencoders," *Neural computation*, vol. 23, no. 7, pp. 1661–1674, 2011.
- [22] Y. Song, J. Sohl-Dickstein, D. P. Kingma *et al.*, "Score-based generative modeling through stochastic differential equations," *arXiv preprint arXiv:2011.13456*, 2020.
- [23] U. S. Kamilov, C. A. Bouman, G. T. Buzzard *et al.*, "Plug-and-play methods for integrating physical and learned models in computational imaging," *arXiv preprint arXiv:2203.17061*, 2022.
- [24] S. Lyu, "Interpretation and generalization of score matching," *arXiv preprint arXiv:1205.2629*, 2012.
- [25] J. R. Chand and M. Jacob, "Plug-and-play deep energy model for inverse problems," *arXiv preprint arXiv:2302.11570*, 2023.
- [26] G. Gasso, A. Rakotomamonjy, and S. Canu, "Recovering sparse signals with a certain family of nonconvex penalties and dc programming," *IEEE Transactions on Signal Processing*, vol. 57, no. 12, pp. 4686–4698, 2009.
- [27] L. Brugnano and F. Iavernaro, *Line integral methods for conservative problems*. CRC Press, 2016, vol. 13.
- [28] L. Bungert, R. Raab, T. Roith *et al.*, "Clip: Cheap lipschitz training of neural networks," in *International Conference on Scale Space and Variational Methods in Computer Vision*. Springer, 2021, pp. 307–319.
- [29] E. Ryu, J. Liu, S. Wang *et al.*, "Plug-and-play methods provably converge with properly trained denoisers," in *International Conference on Machine Learning*. PMLR, 2019, pp. 5546–5557.
- [30] U. S. Kamilov, C. A. Bouman, G. T. Buzzard *et al.*, "Plug-and-play methods for integrating physical and learned models in computational imaging: Theory, algorithms, and applications," *IEEE Signal Processing Magazine*, vol. 40, no. 1, pp. 85–97, 2023.
- [31] Y. Sun, P. Babu, and D. P. Palomar, "Majorization-minimization algorithms in signal processing, communications, and machine learning," *IEEE Transactions on Signal Processing*, vol. 65, no. 3, pp. 794–816, 2016.
- [32] J. Zbontar, F. Knoll, A. Sriram *et al.*, "fastmri: An open dataset and benchmarks for accelerated mri," *arXiv preprint arXiv:1811.08839*, 2018.
- [33] T. Miyato, T. Kataoka, M. Koyama *et al.*, "Spectral normalization for generative adversarial networks," *arXiv preprint arXiv:1802.05957*, 2018.
- [34] B. Levac, A. Jalal, K. Ramchandran *et al.*, "Conditional score-based reconstructions for multi-contrast mri," *arXiv preprint arXiv:2303.14795*, 2023.
- [35] A. Pramanik, S. Bhave, S. Sajib *et al.*, "Adapting model-based deep learning to multiple acquisition conditions: Ada-modl," *arXiv preprint arXiv:2304.11238*, 2023.
- [36] Z.-X. Cui, C. Cao, S. Liu *et al.*, "Self-score: Self-supervised learning on score-based models for mri reconstruction," *arXiv preprint arXiv:2209.00835*, 2022.
- [37] A. Jalal, M. Arvinte, G. Daras *et al.*, "Robust compressed sensing mri with deep generative priors," *Advances in Neural Information Processing Systems*, vol. 34, pp. 14938–14954, 2021.
- [38] G. Luo, M. Blumenthal, M. Heide *et al.*, "Bayesian mri reconstruction with joint uncertainty estimation using diffusion models," *Magnetic Resonance in Medicine*, 2023.
- [39] Y. Nesterov, *Introductory lectures on convex optimization: A basic course*. Springer Science & Business Media, 2003, vol. 87.
- [40] M. Razaviyayn, M. Hong, and Z.-Q. Luo, "A unified convergence analysis of block successive minimization methods for nonsmooth optimization," *SIAM Journal on Optimization*, vol. 23, no. 2, pp. 1126–1153, 2013.